ACS Partner Journal

CHEMICAL & BIOMEDICAL IMAGING

Open Access

pubs.acs.org/ChemBioImaging

Article

Modeling the Thermoelastic Sample Response for Subdiffraction Infrared Spectroscopic Imaging

Published as part of Chemical & Biomedical Imaging virtual special issue "Sub-diffraction Chemical Imaging".

Seth Kenkel and Rohit Bhargava*

Cite This: *Chem. Biomed. Imaging* 2024, 2, 413−421

Read Online

ACCESS | Metrics & More | Article Recommendations | Supporting Information

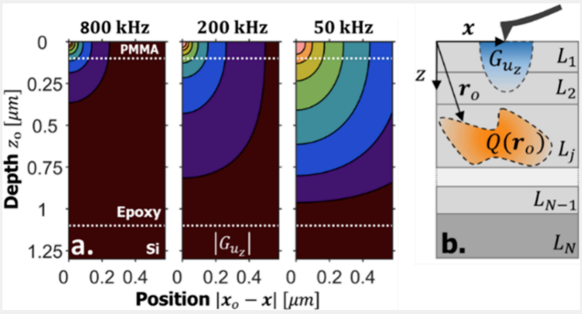

ABSTRACT: There is significant and increasing interest in using the photothermal effect to record infrared (IR) absorption spectra localized to volumes that are considerably smaller than the wavelength of excitation, i.e., subdiffraction imaging. As opposed to conventional IR microscopy, in which absorption and scattering of the illuminating light is measured, subdiffraction imaging can be achieved through detection of the sample's thermal response to IR absorption-induced heating. While this relationship has been examined by a variety of coarse-grained models, a generalized analysis of the dependence of temperature and surface deformation arising from an absorber below the surface has not been reported. Here, we present an analytical model to understand a sample's thermoelastic response in photothermal measurements. The model shows important dependence of the ability to record subdiffraction data on modulation frequency of exciting light, limitations imposed by optical sensing, and the potential to discern location of objects ultimately limited by noise and sharpness of the detecting mechanism. This foundational analysis should allow for better modeling, understanding, and harnessing of the relationship between absorption and sample response that underlies IR photothermal measurements.

KEYWORDS: *photothermal, spectroscopy, thermoelasticity, super-resolution, infrared, AFM-IR*

■ INTRODUCTION

Diffraction and resolving power of optical microscopes are intimately connected, with this phenomenon often cited as the default limiting condition for quality of images that can be recorded. Quantifying resolution by using objective criteria to characterize the overlap in diffraction patterns has become the de facto standard for almost all microscopy in the electromagnetic spectrum to analyze performance. In its simplest form, diffraction-limited resolution is the ability to separate two point sources of contrast in the focal plane of a microscope with a specific numerical aperture and wavelength of light used for imaging. Indeed, the same arguments were long made to understand the limits of resolution in infrared (IR) spectroscopic imaging[1,2] but rigorous analytical models have helped design new instruments with optimal resolving power.[3,4] Moreover, there are several methods to exceed the far-field detection performance beyond the limit defined by common optical components. In the IR, an accessible method is to increase the numerical aperture by using a solid immersion lens.[5−12] Other common techniques from optical microscopy can also be adopted such as introducing additional angular diversity with structured illumination microscopy[13,14] using an IR transparent light projector.[15]

Provided additional information beyond far-field IR measurements at a single wavelength, sample information can potentially be recovered beyond the diffraction-limited resolution. For instance, with IR imaging, two morphologic units to be separated may not be spectrally identical and additional, higher-resolution contrast may be available by considering spectral differences. An important emerging direction in IR imaging, thus, is to understand the role of spectral contrast and signal-to-noise ratio (SNR) of the data and their effect on apparent resolution,[16] i.e., information-limited resolution. Another approach is to use the information from visible imaging combined with computational methods, especially the emerging techniques of deep learning, to enhance IR imaging resolution to match that of a corresponding optical image.[17] This approach, however, relies on prior information or typical structure extrapolated from similar samples and may not provide universally reliable

Received: February 9, 2024
Revised: April 18, 2024
Accepted: April 24, 2024
Published: April 29, 2024

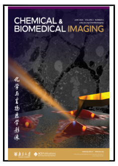

subdiffraction information with the same confidence as directly recorded data. Last, subdiffraction imaging, in principle, can also be achieved for samples with sparsely distributed absorbers or by using subwavelength specialized reporters combined with computational techniques to recover their positions. The computational ability to obtain subdiffraction localization within the same focal spot using a computational reconstruction approach has been proposed[18] but not yet implemented.

Subdiffraction IR imaging can also be achieved by reducing the wavelength of detected light to the visible regime to measure the consequence of absorption upon illumination with IR light, i.e., the sample's thermal response to IR absorption-induced heating. Photothermal imaging[19−24] relies on the thermal-induced optical changes of the sample and can achieve optical resolution, which is subdiffraction compared to the exciting, IR light.[25] This approach relies on more complex instruments and the signal generated depends on the thermal, optical, and elastic response of the material. Further, an excellent approach to harnessing similar photothermal effects for subdiffraction measurements is to use atomic force microscopy (AFM) to record signals proportional to the IR photoinduced expansion.[26−37] With AFM-IR, the sample is illuminated with a modulated IR source, which causes periodic heating upon light absorption, and the local sample response is sensed using a cantilever with a sharp tip. Hence, this approach potentially offers resolution up to the radius of the AFM tip. However, it is not clear whether that limiting performance may be achievable if the absorber is not close to the surface.[32,38] Further, it has only recently become possible to separate the mechanical and chemical contributions[39] to measured signal as well as to obtain high SNR data using null deflection IR imaging.[38,40] Thus, it becomes timely to examine the limiting factors underlying resolution when data is not limited by SNR and other factors.

In this manuscript, we consider photothermal approaches to subdiffraction IR imaging and seek to develop an analytical framework that allows us to relate the observed sample deformation to local absorption. While the recorded photothermal data is a result of both the optical and mechanical properties of the sample, we focus our modeling efforts here on improved understanding of the thermoelastic sample response. Subsequently, the limits imposed by optical or AFM sensing can be imposed and the performance of the entire setup estimated. Several studies have examined image formation using the photothermoelastic response[41−43] as well as image formation in microscopy and nanoscopy.[26,28,44] However, an analytical model to relate an arbitrary distribution of IR absorbing material in a sample and its impact on achievable resolution is needed. Here, we provide this analytical model to predict the thermoelastic response of the sample by an absorber placed its volume and relate it to image resolution via spatial frequency analysis of the deformation. Our aim is to understand the true potential for super resolution imaging, beyond the sensing limits of optical diffraction or AFM tip sizes, such that better understanding of image contrast and future design of high-performance instrumentation is enabled.

■ APPROACH TO ANALYTICAL MODELING OF PHOTOTHERMAL MEASUREMENTS

Our approach is to seek a piecewise solution for temperature and motion in an n-layer half space, subject to arbitrary heating in one layer. Due to linearity of this problem, heating that spans multiple layers can then be analyzed using a superposition of individual layer heating solutions that result from this analysis. This idealized representation is shown in Figure 1a.

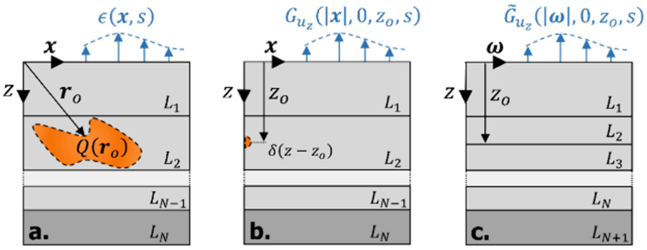

Figure 1. Thermoelastic Green's Function Geometry. (a) N-Layer sample between two semi-infinite domains with arbitrary volumetric heating (shown in layer L_2). (b) The same geometry as (a) with a delta heat source located in L_2. (c) The same configuration as (b) converted to spatial frequency coordinates.

Here, layers (labeled L_1, L_2, etc.) represent different materials, $\boldsymbol{x}$ is lateral position, $\boldsymbol{\omega}$ is the lateral spatial frequency vector (replaces $\boldsymbol{x}$ when in frequency domain), z is depth, $\mathbf{r}_o$ is position vector of the heating function Q, ϵ is expansion, s is Laplace variable, G_{u_z} and $\tilde{G}_{u_z}$ are the Green's functions in spatial and frequency domain respectively, and δ is the dirac delta function. Volumetric heat generation $Q(\mathbf{r}_o)$, induced by IR absorption or otherwise, is defined as a function of $\mathbf{r}_o = [x_o, y_o, z_o]$ and would result in a local temperature increase and dilation of the sample. This would cause vertical motion of the surface, $\epsilon(\mathbf{x}, s)$. Note, because many photothermal methods utilize heterodyne detection combined with pulsed IR lasers (i.e., harmonic solutions), we restrict our solutions to temporal frequency domain using Laplace transform as this offers a general definition and provides a more natural representation of harmonic heating. The solution for arbitrary heating requires defining a Green's Function, G_{u_z}, which relates the vertical motion of material at any arbitrary position in the half-space in response to a kernel heat source (i.e., delta function) at depth z_o shown in Figure 1b. Note, if the equations were in time domain, the delta function (invariant in time and lateral position) would have the form $\delta(\boldsymbol{x})\delta(z - z_{o'})\delta(t)$ where t is time. After transforming to Laplace domain, this becomes $\delta(\boldsymbol{x})\delta(z - z_{o'})$ since the Laplace transform of $\mathcal{L}\{\delta(t)\} = 1$. This is sometimes called a transfer function (instead of Green's function) when applied to time-domain.[39] Further, it is also common to seek a harmonic solution which would fix the temporal form to a harmonic function $\delta(\boldsymbol{x})\delta(z - z_{o'})e^{-i\omega t}$. Here, we will use the Laplace domain delta function of the form $\delta(\boldsymbol{x})\delta(z - z_{o'})$. All equations hereafter will be described in Laplace domain.

Provided a linear system of equations relating Thermoelastic effects to heating, solving the system for delta heat source would yield the desired Green's function.[45] For instance, the general solution for surface expansion can be written as

$$\epsilon(\mathbf{x}, s) = \iiint_{\Omega} G_{u_z}(\mathbf{x}, \mathbf{x_o}, 0, z_o, s) Q(\mathbf{x_o}, z_o) d\mathbf{x_o} dz_o \qquad (1)$$

The governing equations to derive the spatial form of the Green's function $G_{u_z}(\mathbf{x}, \mathbf{x}_o, z, z_o, s)$ written here requires solving a Partial Differential Equation (PDE) which is difficult to do analytically. Instead, we seek to develop an analytical description by considering an idealized representations that are reflective of common samples. First, consider that biological domains often are large (relative to thickness) and have very similar properties. Thus, our first simplification is to assume that material properties (except IR absorption) are invariant in the **x** coordinate. Due to the film-like geometry, the Green's function becomes spatially invariant in **x** (i.e., $\mathrm{G}_{u_z}(\mathbf{x} - \mathbf{x_o}, z, z_o, \mathrm{s}))$ and we can convert to spatial frequency domain via a 2D Fourier transform, resulting in form shown in Figure 1c. The general solution in spatial frequency form becomes the following

$$\tilde{\mathrm{e}}(\boldsymbol{\omega}, \mathrm{s}) = 2\pi \int_{\Omega} \tilde{\mathrm{G}}_{u_z}(|\boldsymbol{\omega}|, 0, z_o, \mathrm{s})\tilde{\mathrm{Q}}(\boldsymbol{\omega}, z_o)\mathrm{d}z_o \tag{2}$$

Here, we applied the 2D unitary, angular frequency Fourier transform to the lateral spatial coordinates **x** assuming the Green's function is spatially invariant (i.e., $\mathcal{F}\left\{ \iint_{\Omega} f(\mathbf{x} - \mathbf{x_o})\mathrm{g}(\mathbf{x_o})\mathrm{d}\mathbf{x_o} \right\} = 2\pi\tilde{\mathrm{f}}(\boldsymbol{\omega})\tilde{\mathrm{g}}(\boldsymbol{\omega})$). See Supporting Information (SI) Note 1 for more details. The spatial form $\epsilon(\mathbf{x}, s)$ of interest can be determined by applying an inverse Fourier transform of $\tilde{\epsilon}(\boldsymbol{\omega}, s)$ or a discrete Fourier transform when the function is represented as sampled points of the expansion field (i.e., photothermal images). The major benefit of this form, the function $\tilde{G}_{u_z}(|\boldsymbol{\omega}|, z, z_o, s)$ is the solution to a system of ordinary differential equations for each layer coupled via thermoelastic conditions at each interface. The governing behavior of each layer and coupling conditions at interfaces will be derived next.

DESCRIBING THE THERMOELASITY GOVERNING BEHAVIOR

The governing equations for the thermoelastic response of a sample subject to a point heat source (i.e., Green's function) is as follows[46]

$$\begin{gathered} \mu_i \nabla^2 \mathbf{u}_i + (\lambda_i + \mu_i)\nabla(\nabla \cdot \mathbf{u}_i) = \gamma_i \nabla T_i, \\ \nabla^2 T_i - \frac{\mathrm{s}}{\alpha_i} T_i = -\frac{1}{k_i}\delta(\mathbf{x}, z - z_o) \end{gathered} \tag{3}$$

Here, for the i^{th} layer of Figure 1, μ_{I} is the shear modulus, λ_i is Lamé's first parameter, α_{i} is the thermal diffusivity, k_i is the thermal conductivity, $\mathbf{u}_{\mathrm{i}}$ is the displacement vector, and T_{i} is the temperature. The parameter γ_{i} is a grouped term to simplify the equations and equals $(3\lambda_{\mathrm{i}} + 2\,\mu_{\mathrm{i}})\,\beta_{\mathrm{i}}$ where β_{i} is the linear thermal expansion coefficient. Additionally, the inertia term $\rho_i \frac{\partial^2 \mathbf{u}_{\mathrm{i}}}{\partial t^2}$ was omitted due to the small length scale of most samples relative to acoustic wavelengths. The Green's function $\mathrm{G}_{\mathrm{u}_z}$ from before is equal to $\mathbf{u}_{\mathrm{i}} \bullet \hat{k}$ where $\hat{k}$ is the unit vector in the z-direction from Figure 1b. Solving for the displacement vector field $\mathbf{u}_{\mathrm{i}}$ is often achieved through decomposition into potential fields.[46] Here, for simplicity, we will assume a common form as follows

$$\mathbf{u}_i = \nabla\phi_i \tag{4}$$

Here, we chose a reduced form of the Helmholtz decomposition[46] for simplicity with one scalar potential field. Although this does not provide a general form, we will later provide constraints to validate this choice. Applying this decomposition to eq 3, the governing equations of thermoelasticity reduce to the following

$$\begin{gathered} \nabla^2\phi_i = m_i T_i, \\ \nabla^2 T_i - \frac{s}{\alpha_i} T_i = -\frac{1}{k_i}\delta(\mathbf{x}, z - z_o) \end{gathered} \tag{5}$$

Here, $\mathrm{m_i}$ is another grouped term equal to $\frac{\gamma_i}{\lambda_i + 2\mu_i}$. To complete the model, we have to now consider 4 constraints that must be satisfied at any interface between 2 dissimilar materials as follows

$$\begin{aligned} \mathbf{u}_i|_{z=d_i} &= \mathbf{u}_{i+1}|_{z=\mathrm{d}_i}, \\ \boldsymbol{\sigma}_i \cdot n\hat{}|_{z=d_i} &= \boldsymbol{\sigma}_{i+1} \cdot n\hat{}|_{z=d_i}, \\ T_i|_{z=d_i} &= T_{i+1}|_{z=d_i}, \\ \boldsymbol{q}_i \cdot n\hat{}|_{z=d_i} &= \boldsymbol{q}_{i+1} \cdot n\hat{}|_{z=d_i} \end{aligned} \tag{6}$$

Here, for the i^{th} layer, $\boldsymbol{\sigma}_i$ is the stress tensor, $\boldsymbol{q}_i$ is the heat flux vector, d_i is the depth of the interface between layers i and i+1, and $\hat{n}$ is the normal vector of said interface. The fields in adjacent layers at each interface must have matching temperature, heat flux, displacement, and stresses (along the interface normal). To write these 4 conditions explicitly in terms of the potential and temperature fields, we must first write the stress tensor and heat flux vector for a thermoelastic material defined as follows[46]

$$\begin{gathered} \boldsymbol{\sigma} = 2\mu\boldsymbol{\epsilon} + (\lambda \mathrm{tr}(\boldsymbol{\epsilon}) - \gamma \mathrm{T})\boldsymbol{\delta}, \\ \boldsymbol{\epsilon} = \frac{1}{2}(\nabla\mathbf{u} + \nabla\mathbf{u}^{\mathbf{T}}) \\ \boldsymbol{q}_i = k_i \nabla T_i \end{gathered} \tag{7}$$

Here, $\boldsymbol{\delta}$ is the Kronecker delta, $\mathrm{tr}(\boldsymbol{\epsilon})$ is the trace of tensor $\boldsymbol{\epsilon}$, and $\nabla\mathbf{u}^{\mathbf{T}}$ is the transpose of $\nabla\mathbf{u}$. Applying this definition in cylindrical coordinates using eq 4, the conditions of eq 6 are as follows

$$\begin{gathered} \mathbf{B}_i|_{z=d_i} = \mathbf{B}_{i+1}|_{z=d_i}, \\ \mathbf{B}_i|_{z=d_i} = \begin{bmatrix} \dfrac{\partial\phi_i}{\partial r} \\ \dfrac{\partial\phi_i}{\partial z} \\ \mu_i \dfrac{\partial}{\partial z}\left(\dfrac{\partial\phi_i}{\partial r}\right) \\ \mu_i\left(\dfrac{1}{r}\dfrac{\partial}{\partial r}\left(r\dfrac{\partial\phi_i}{\partial r}\right)\right) \\ T_i \\ k_i \dfrac{\partial T_i}{\partial z} \end{bmatrix} \end{gathered} \tag{8}$$

For more details regarding this result, see SI note 1. At this stage, we redefined the lateral coordinates $\boldsymbol{x}$ in cylindrical coordinates with radius r due to the axis symmetry of this problem. The scalar potential field ϕ_i defined previously does not provide sufficient degrees of freedom to satisfy these constraints. For simplicity, instead of defining additional potential functions to satisfy these constraints exactly, for simplicity, we will assume each layer has constant shear modulus μ_i. Provided this assumption, only two unique interface conditions are now required for the scalar potential field ϕ_i. Applying this assumption, the temperature and dilation fields can be determined using the following system

$$\begin{gathered}\nabla^2\phi_i = m_i T_i,\\ \nabla^2 T_i - \frac{s}{\alpha_i}T_i = -\frac{1}{k_i}\delta(\mathbf{x}, z - z_o),\\ \phi_i|_{z=d_i} = \phi_{i+1}|_{z=d_i},\\ \frac{\partial\phi_i}{\partial z}|_{z=d_i} = \frac{\partial\phi_{i+1}}{\partial z}|_{z=d_i},\\ T_i|_{z=d_i} = T_i|_{z=d_i},\\ k_i\frac{\partial T_i}{\partial z}|_{z=d_i} = k_{i+1}\frac{\partial T_i}{\partial z}|_{z=d_i}\end{gathered} \tag{9}$$

The solution to this system, although restricted to N-layer film domains with constant shear modulus, provides a complete system for characterizing relevant thermoelastic effects in photothermal measurements, i.e., quantifying temperature and vertical sample motion anywhere in the N-layer sample in response to arbitrary distributions of IR absorption. Although temperature can be solved directly from eq 9), the potential ϕ_i currently depends on the temperature field. One approach is to solve for the temperature and the potential ϕ_i (as a function of temperature) separately and then apply a convolution of the two to determine the Green's function relating ϕ_i directly to heat generation (i.e., IR absorption); however, the final convolution will be difficult to perform analytically. Instead, we can combine the two second order systems into one-fourth order for a direct solution of ϕ_i as follows

$$\begin{gathered}\nabla^2\nabla^2\phi_i - \frac{s}{\alpha_i}\nabla^2\phi_i = -\frac{m_i}{k_i}\delta(\mathbf{x}, z - z_o),\\ \phi_i|_{z=d_i} = \phi_{i+1}|_{z=d_i},\\ \frac{\partial\phi_i}{\partial z}|_{z=d_i} = \frac{\partial\phi_{i+1}}{\partial z}|_{z=d_i},\\ \frac{1}{m_i}\nabla^2\phi_i|_{z=d_i} = \frac{1}{m_{i+1}}\nabla^2\phi_{i+1}|_{z=d_i},\\ \frac{k_i}{m_i}\frac{\partial\nabla^2\phi_i}{\partial z}|_{z=d_i} = \frac{k_{i+1}}{m_{i+1}}\frac{\partial\nabla^2\phi_{i+1}}{\partial z}|_{z=d_i}\end{gathered} \tag{10}$$

Here, we used the first relation of eq 9 to eliminate temperature from the governing equations. This system describes the governing behavior for ϕ_i directly from heating without the need to solve for temperature. Temperature can then be determined easily with derivatives of the potential ϕ_i using the first relation in eq 9 if desired. There are 4 more conditions at z equal to zero and infinity to close these equations defined as follows

$$\begin{gathered}\phi_1|_{z=0} = 0.\quad \lim_{z\to\infty}\frac{\partial\phi_n}{\partial z} = 0,\\ \frac{\partial\nabla^2\phi_i}{\partial z}|_{z=0} = 0.\quad \lim_{z\to\infty}\nabla^2\phi_n = 0\end{gathered} \tag{11}$$

These conditions define a stress-free, perfectly insulating surface with displacement and temperature fields that converge to zero at infinite depth. The displacement field $\mathbf{u}_i$ can be computed directly using ϕ_i and eq 4 without the need to solve for temperature. Temperature can be determined directly from ϕ_i using $\nabla^2\phi_i = m_i T_i$.

■ DERIVATION OF THE PHOTOTHERMAL EXPANSION GREEN'S FUNCTIONS

The proposed equations provide a complete model for temperature and sample displacement for an N-layer film half space with constant shear modulus. Hereafter, we will restrict our analysis to vertical displacement solutions for discussion purposes. The vertical displacement Green's solution can be determined by applying a 2D Fourier transform to eq 10, resulting in the following

$$\frac{\partial^4\tilde{\phi}_i}{\partial z^4} - \left(2\rho^2 + \frac{s}{\alpha_i}\right)\frac{\partial^2\tilde{\phi}_i}{\partial z^2} + \left(\rho^4 + \frac{s}{\alpha_i}\rho^2\right)\tilde{\phi}_i = -\frac{m_i}{2\pi k_i}\delta(z - z_o) \tag{12}$$

The potential $\tilde{\phi}_i$ is the frequency domain representation of the scalar potential which is a function of spatial frequency parameter $\rho = |\boldsymbol{\omega}|$. The delta function at plane z_o on the right can be treated as another interface if we change the interface conditions from eq 10 to the following

$$\begin{gathered}\mathbf{B}_i|_{z=d_i} = \mathbf{B}_{i+1}|_{z=d_i} + \frac{1}{2\pi}\delta_{ij}\mathbf{D},\\ \mathbf{B}_i = \begin{bmatrix}\tilde{\phi}_i\\ \frac{\partial\tilde{\phi}_i}{\partial z}\\ \frac{1}{m_i}\left(\frac{\partial^2\tilde{\phi}_i}{\partial z^2} - \rho^2\tilde{\phi}_i\right)\\ \frac{k_i}{m_i}\left(\frac{\partial^3\tilde{\phi}_i}{\partial z^3} - \rho^2\frac{\partial\tilde{\phi}_i}{\partial z}\right)\end{bmatrix},\quad \mathbf{D} = \begin{bmatrix}0\\0\\0\\1\end{bmatrix}\end{gathered} \tag{13}$$

For more details into this result, see SI note 1. In short, we applied the 2D Fourier transform to the interface conditions of eq 10 and added an additional condition (represented by $\mathbf{D}$) to account for heat generation within a new interface created in the heating layer (j^{th} layer). This interface splits the heating layer into two, increasing the total layer count by one. For example, when the heating layer is the first layer, the first layer is split into two separate layers increasing the total layer count by 1 adding an interface that exhibits heat generation. In this example, the "first" and "second" layer (two halves that were split) have identical material properties but will incorporate interface heating $\mathbf{D}$ since the $\delta_{11} = 1$. The interface relation for the new first and second layers is $\mathbf{B}_1|_{z=d_i} = \mathbf{B}_2|_{z=d_i} + \frac{1}{2\pi}\mathbf{D}$ whereas, for all other layers, $\delta_{n1} = 0$ and $\mathbf{D}$ is omitted. Subject to this new geometry and interface condition, the governing behavior of eq 12 now becomes homogeneous (i.e., no delta source of heating within any layer). The general solution to the

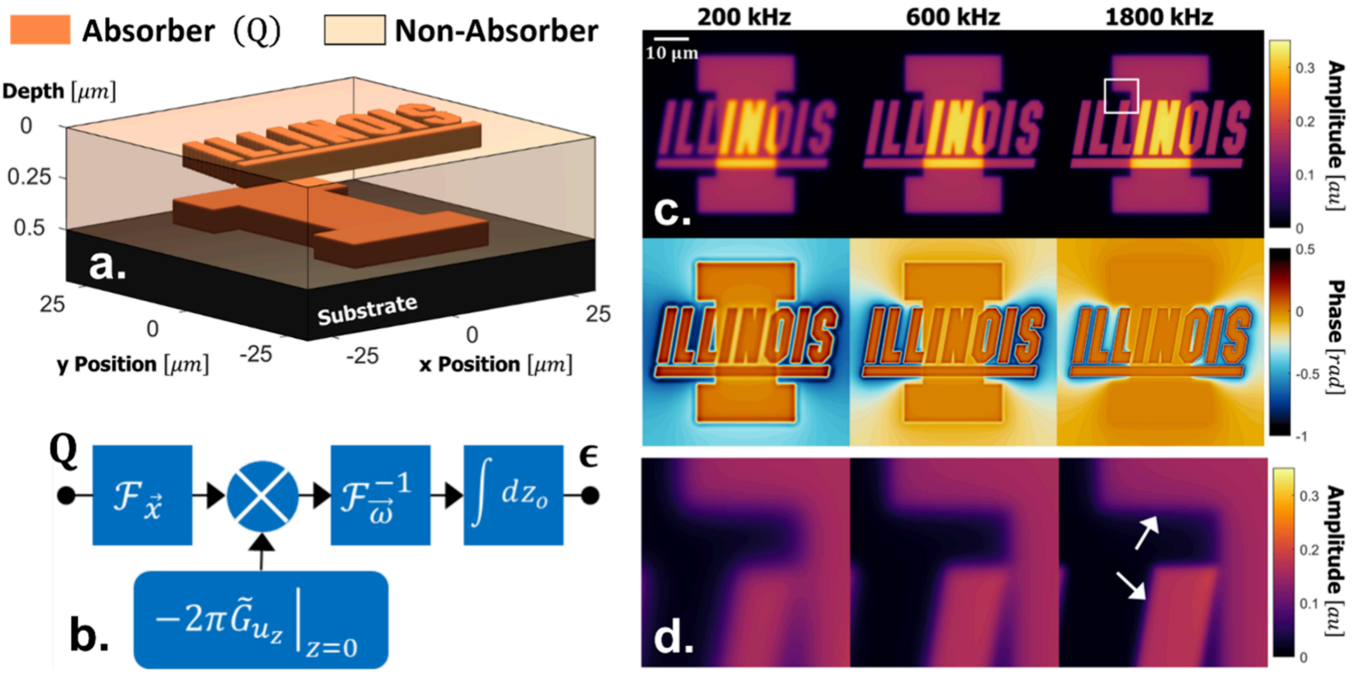

Figure 2. Modeling harmonic expansion. (a) Schematic of simulated spatial domain with Illinois and block-I volumetric heat sources. (b) Schematic of the simulation workflow. Here, 2D Fourier transforms are represented by $\mathcal{F}_{\vec{x}}$. (c) Thermal expansion amplitude (top row) and phase (middle row) with outputs for 200 kHz, 600 kHz, and 1800 kHz for a PMMA film on a PMMA substrate (i.e., a PMMA half space). (d) Zoom regions (bottom row) of the white box from (c).

homogeneous form of eq 12 can now be written explicitly as follows

$$\tilde{\phi}_i = c_{4i-3}\mathrm{e}^{\sqrt{\rho^2+\frac{s}{\alpha_i}}z} + c_{4i-2}e^{-\sqrt{\rho^2+\frac{s}{\alpha_i}}z} + c_{4i-1}e^{\rho z} + c_{4i}e^{-\rho z} \tag{14}$$

For more details, see SI note 1. The general solution results in 4 * $(n + 1)$ unknown coefficients defined as c for all the layers of Figure 1c. The interface conditions of eq 13 provides $4n$ equations. The remaining four equations come from conditions at the surface and infinite depth defined as follows

$$\phi_1|_{z=0} = 0, \qquad \lim_{z\to\infty} \frac{\partial \phi_n}{\partial z} = 0,$$
$$\left(\frac{\partial^3 \tilde{\phi}_1}{\partial z^3} - \rho^2 \frac{\partial \tilde{\phi}_1}{\partial z}\right)\Big|_{z=0} = 0, \quad \lim_{z\to\infty}\left(\frac{\partial^2 \tilde{\phi}_n}{\partial z^2} - \rho^2 \tilde{\phi}_n\right) = 0 \tag{15}$$

The final vertical displacement Green's function is a piecewise description of these potential functions defined as follows

$$G_{\sim u_z}(\rho, z, z_o, s) = \sum_{i=1}^{N+1} \frac{\partial \tilde{\phi}_i(\rho, z, z_o, s)}{\partial z}(H(z - d_{i-1}) - H(z - d_i)) \tag{16}$$

Here, the function H is the Heaviside step function. The vertical displacement Green's function solution can be computed programmatically using symbolic math libraries in Matlab or Mathematica.

■ SIMULATING PHOTOTHERMAL EXPANSION MEASUREMENTS

Photothermal imaging techniques such as AFM-IR[38−40] and IR optical hybrid (IROH)[47] microscopies demodulate the harmonic expansion of the sample surface induced by IR heating. The model proposed here can be adapted to describe the harmonic amplitude and phase images produced by these measurements by simply substituting the Laplace variable s for $i\omega$ where ω is the repetition rate of the laser in $\left[\frac{\text{rad}}{\text{s}}\right]$. Simulations can be conducted by defining a 3D matrix of heating sampled in spatial coordinates. Here, we examine a sample with Illinois and block-I absorbing features (i.e., sources of volumetric heating) as shown in Figure 2a. Simulations of expansion can be conducted for samples of this type following the schema in Figure 2b. The heating matrix is converted to spatial frequency domain with a discrete Fourier transform (DFT), multiplied by the Green's function (sampled at the same spatial frequencies as the heating matrix), converted back to spatial coordinates with an inverse DFT, and subsequently integrated along the z dimension. The amplitude and phase images produced by a photothermal expansion lock-in measurement are equal to the amplitude and phase of the model output, respectively.

Figure 2c shows simulations of the vertical expansion amplitude and phase at 200 kHz, 600 kHz, and 1800 kHz. Here, the complex expansion was scaled by Laplace variable $s = i2\pi f$ to normalize each image by their DC component (raw images are provided in SI note 2) and reveals several interesting features of the sample response that are important for photothermal detection. First, the recorded signal has a frequency dependence that changes with the depth of the absorbing feature resulting from thermal diffusion. For example, the phase of the block I signal nearly disappears at 1800 kHz due to the low thermal diffusion length associated at high frequencies. This suggests there is unique information contained in the frequency dimension for distinguishing material at different depths. Lateral resolution also appears to become enhanced at higher frequencies which is more apparent in the zoom regions of Figure 2d. This is also attributable to thermal diffusion, which depends on modulation frequency. These subtle variations in expansion behavior are potentially rich with useful depth information about the sample; however, extracting this information is not straightforward. For example, provided the assumptions of a half-space with constant material properties and a perfectly insulating surface, expansion measurements cannot be used to distinguish film-like absorbers at different depths. For film-like samples that contain only DC spatial frequencies, expansion is simply equal to the integral of temperature (or energy) applied to the half space without any dependence on depth.[39,47,48] Although this energy spreads over time due to thermal diffusion, the resulting expansion (or integral of energy in depth) remains constant no matter the distribution of this energy within the half space since this energy has no way to dissipate. This is obviously not true in practice as acoustics, surface losses, nonlinearities, and layered materials introduce additional, unique relations between frequency and depth. It is unclear whether the addition of these model elements would enable depth sensing of films using detection configured to record sample expansion. We note, for photothermal methods that record signal proportional to temperature, such as temperature dependent changes in optical scattering at interfaces,[49] the DC temperature signal produced by films may have unique depth dependence allowing for recovery of film IR absorption at different depths. Regardless, any inverse algorithm developed to map IR absorption in 3D using photothermal expansion would yield a passband of spatial frequencies and utilize the subtle changes in lateral blurring and phase observed in Figure 2.

We note that similar behavior has been observed previously as efforts to distinguish IR contrast at different depths using modulation frequency have been previously successful. Scanning near field optical microscopy (SNOM) techniques,[50−52] for example, harness different harmonic frequencies using AFM tapping mode to distinguish scattered light from surface and subsurface materials. As opposed to SNOM methods, sensing photothermal effects for resolution enhancement has several advantages. For instance, the penetration depth is only dependent on the frequency, whereas SNOM methods will ultimately be confined to depths proportional to the radius of the AFM tip. This offers more tunability by adjusting the pulsing frequency targeted to the desired depth of interest. Additionally, the effects presented here are independent of the detection method. We emphasize that the same depth recovery methods can be described linearly with analytical modeling shown here and applied directly to all photothermal detection methods such as AFM and visible microscopy. The relative simplicity of this mechanism and its versatility offer significant potential for super resolution IR imaging. To illustrate this potential, we examine the limiting performance defined by this model compared to the diffraction- or tip-limited cases next.

RESOLUTION LIMITS DICTATED BY THE THERMOELASTIC RESPONSE

The diffraction limit defines the lowest spatial frequency that can be measured from a distance with a conventional microscope. This feature of an optical system is characterized by the modulation transfer function (MTF) which describes the magnitude of the amplitude of periodic features as a function of spatial frequency. For an ideal, far-field, incoherent imaging system with a circular pupil, the modulation transfer function is defined as follows[53]

$$\mathrm{MTF}(\rho) = \begin{cases} \left| \dfrac{2}{\pi}\left(\mathrm{acos}\left(\dfrac{\rho}{2\rho_\mathrm{o}}\right) - \dfrac{\rho}{2\rho_\mathrm{o}}\sqrt{1-\left(\dfrac{\rho}{2\rho_\mathrm{o}}\right)^2}\right)\right| & \rho \le 2\rho_\mathrm{o} \\ 0 & \text{otherwise} \end{cases},$$
$$\text{where } \rho_\mathrm{o} = \frac{2\pi w}{\lambda z_i} \tag{17}$$

Here, ρ is the spatial frequency in [rad/mm], w is the radius of the circular pupil, z_i is the image distance/focal length, and λ is the wavelength in [1/mm]. Note, this formula is a piecewise function that exhibits a finite limit to the propagation of spatial frequencies at $2\rho_\mathrm{o}$ due to the nature of far-field detection where ρ_o is the optical cutoff frequency. Figure 3a below shows a comparison between the far-field IR (red), far-field visible (green), and thermoelastic effect-limited (blue) MTF curves. Note, here, we are assuming the detection of the thermoelastic response exhibits resolving potential well beyond far-field diffraction limit such as detection of near-field thermoelastic expansion using AFM-IR. The diffraction-limited absorption (at 6 μm) for IR imaging shows the weakest resolving power of the three and deviates from the thermoelastic limit rapidly, as expected. Interestingly, for visible detection, the thermoelastic limit at this modulation frequency allows for nearly optical-limited tracking of the spatial frequencies. The thermoelastic MTF itself does not exhibit a sharp, limiting cutoff frequency as with the far-field measurements. This makes defining resolution of a photothermal system different than traditional

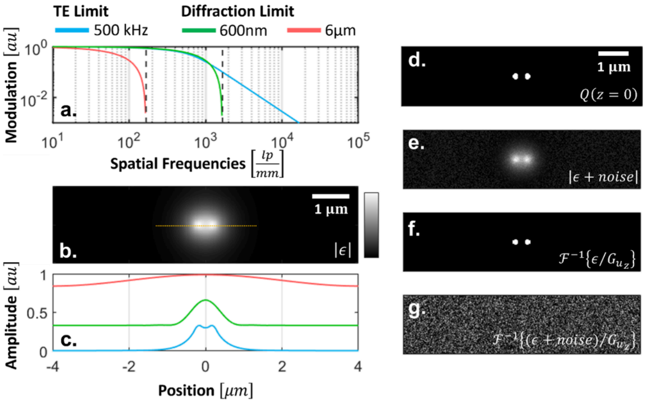

Figure 3. Thermoelasticity resolution limits. (a) Modulation transfer functions (MTF) of far-field IR optics (red), visible optics (green), and thermoelastic response (blue). IR and visible optics were simulated using 10 μm and 600 nm light respectively with NA = 0.7. Thermoelastic response was simulated using geometry from Figure 2 at 500 kHz for a surface point absorber. (b) Same thermoelastic simulation from (a) of two 200 nm diameter beads separated by 200 nm. (c) Line profiles across the beads along dashed line from (b) with the thermoelastic simulation (blue) and simulations of far-field optical transfer function (OTF) for wavelengths 600 nm (green) and 6 μm (red). Plots are normalized to maximum and offset for clarity. (d) Same geometry as (b) with heating defined only at $z = 0$ with distribution shown here. (e) Expansion amplitude plus noise using heating from (d). (f) and (g) Wiener deconvolution of expansion from (e) assuming zero noise and noise, respectively. For error free measurements with heating confined to an infinitesimal thin layer, all spatial frequencies of heating Q can be recovered.

optical systems that incorporate the Rayleigh criteria, as is common for far-field optical detection and is the basis for an opportunity to exceed diffraction limits from visible or IR light.

For near-field detection, using an AFM tip for example, the lack of a sharp cutoff frequency suggests the possibility of arbitrary IR resolution up to physical limits of the detection. For instance, Figure 3b shows a simulation of the thermoelastic response of two beads spaced 100 nm apart, revealing expansion amplitude signal with a minimum at their midpoint. This same dip is not present in simulations of far-field measurements of a visible microscope shown in the green plot of Figure 3c even though both have similar spread in signal. In this case, quantifying resolution based on the spread in signal (i.e., the Rayleigh criteria) would underestimate the potential of photothermal detection methods. Although the magnitude of the dip will decrease linearly with the gap distance following the roll-off of the TE limited MTF curve from Figure 3a, it will never be identically zero for finite gaps. Thus, for a system with an infinitesimally small detector, infinite SNR, and zero measurement error; two absorbers can be resolved to any spacing. In practice, however, the resolution will be limited by noise and sources of measurement error such as AFM probe coupling effects.[38,39] This can be shown with a simple simulation in which heating Q is recovered by deconvolution of the simulated expansion. Here, for clarity, we will assume heating is confined to an infinitesimal thin layer located at a finite depth (such as an ultrathin sectioned samples). Figure 3d shows a "cross-section" through the center of the original beads applied to the $z = 0$ plane of the domain with no heating elsewhere. Figure 3e is the resulting expansion amplitude with additional noise typically observed in measurements. Although the noise appears negligible, its effect on recovering the fine, ~100 nm features is significant. Figure 3f and g show the Wiener deconvolution of the expansion measurements for noiseless and noisy measurements, respectively. Simulations here show that error free photothermal measurements have the potential for recovering IR absorption to arbitrary spatial frequencies (resolution) but are highly limited by noise and other measurement error.

For photothermal techniques that rely on far-field optical detection instead of sharp AFM tips, thermoelastic modeling can still provide enhancement in resolution. For instance, recovery of depth information using the frequency/depth relation could be harnessed with optical readout to reduce out-of-focus contrast akin to the difference between confocal and bright field detection. Beyond this effect, it is likely not possible improve image resolution beyond the sharp cutoff frequency of far-field detection without additional information or methods such as hyperspectral data or structured illumination, respectively. Regardless the choice of detection, achieving these ultimate resolution limits requires accurate modeling of the thermoelastic response and an accurate relation to the detected signal. Here, we derived a pseudogeneral, N-layer thermoelastic half space model to highlight the potential benefits of photothermal imaging modalities. While this model significantly advances our understanding, we also note that it is incomplete. One major assumption made in this analysis is the restriction of constant shear modulus to satisfy the stress conditions at interfaces between layers. Introducing arbitrary shear modulus (allowing for arbitrary layered materials) would require an additional potential function that couples with ϕ_i for a general solution. Regardless, the resolution limits and frequency/depth dependence ideas proposed here would not change with this addition. Similarly, more complex optical schemes for illumination and sensing may be used to sense the photothermal response. It is anticipated that this model can serve as a starting point for such future expansions of the theory for subdiffraction IR photothermal imaging.

CONCLUSIONS

Photothermal spectroscopic techniques show great promise for surpassing the diffraction limited resolution of conventional far-field IR imaging. Unlocking the ultimate resolution potential of these methods requires understanding the behavior of the thermoelastic fields and understanding how the detection relates to these fields. Here, we describe a general analytical model for the out-of-plane expansion and temperature in an N-layer film between 2 half space domains to capture the thermoelastic response of most photothermal methods today. With this model, the frequency dependent behavior was shown qualitatively through simulated samples and resolution limits were explored by comparing the MTF curves of thermoelastic and far-field optical responses. While optical methods are limited by diffraction, AFM detection methods have the potential to record much higher resolution and can be enhanced further through modeling provided high-quality measurements. When paired with high quality photothermal measurements, this analytical understanding can help push the limits of resolution to explore ever smaller features in chemical imaging.

ASSOCIATED CONTENT

Supporting Information

The Supporting Information is available free of charge at https://pubs.acs.org/doi/10.1021/cbmi.4c00018.

Detailed derivation of model equations and additional simulations without normalization (PDF)

AUTHOR INFORMATION

Corresponding Author

Rohit Bhargava − *Beckman Institute for Advanced Science and Technology, University of Illinois Urbana−Champaign, Urbana, Illinois 61801, United States; Departments of Bioengineering, Mechanical Science and Engineering, Electrical and Computer Engineering, Chemical and Biomolecular Engineering, and Chemistry and Cancer Center at Illinois, University of Illinois Urbana−Champaign, Urbana, Illinois 61801, United States;* orcid.org/0000-0001-7360-994X; Email: rxb@illinois.edu

Author

Seth Kenkel − *Beckman Institute for Advanced Science and Technology, University of Illinois Urbana−Champaign, Urbana, Illinois 61801, United States*

Complete contact information is available at:
https://pubs.acs.org/10.1021/cbmi.4c00018

Notes

The authors declare no competing financial interest.

ACKNOWLEDGMENTS

Research reported in this publication was supported in part by the National Institute of Biomedical Imaging and Bioengineering of the National Institutes of Health under Award Number

T32EB019944 and R01EB009745. The content is solely the responsibility of the authors and does not necessarily represent the official views of the National Institutes of Health. This work was also supported by NSF grant 2243257, the National Science Foundation Science and Technology Center for Quantitative Cell Biology.

■ REFERENCES

(1) Carr, G. L. Resolution limits for infrared microspectroscopy explored with synchrotron radiation. *Rev. Sci. Instrum.* **2001**, *72* (3), 1613−1619.

(2) Lasch, P.; Naumann, D. Spatial resolution in infrared microspectroscopic imaging of tissues. *Biochimica et Biophysica Acta (BBA) - Biomembranes* **2006**, *1758* (7), 814−829.

(3) Reddy, R. K.; Walsh, M. J.; Schulmerich, M. V.; Carney, P. S.; Bhargava, R. High-definition infrared spectroscopic imaging. *Appl. Spectrosc.* **2013**, *67* (1), 93−105.

(4) Nasse, M. J.; Walsh, M. J.; Mattson, E. C.; Reininger, R.; Kajdacsy-Balla, A.; Macias, V.; Bhargava, R.; Hirschmugl, C. J. High-resolution Fourier-transform infrared chemical imaging with multiple synchrotron beams. *Nat. Methods* **2011**, *8* (5), 413−6.

(5) Fletcher, D. A.; Crozier, K. B.; Quate, C. F.; Kino, G. S.; Goodson, K. E.; Simanovskii, D.; Palanker, D. V. Near-field infrared imaging with a microfabricated solid immersion lens. *Appl. Phys. Lett.* **2000**, *77* (14), 2109−2111.

(6) Breitenstein, O.; Altmann, F.; Riediger, T.; Karg, D.; Gottschalk, V. Lock-in thermal IR imaging using a solid immersion lens. *Microelectronics Reliability* **2006**, *46* (9), 1508−1513.

(7) Michaels, C. A. Mid-infrared imaging with a solid immersion lens and broadband laser source. *Appl. Phys. Lett.* **2007**, *90* (12) DOI: 10.1063/1.2716337.

(8) Kazarian, S. G.; Chan, K. L. A. *Micro- and Macro-Attenuated Total Reflection Fourier Transform Infrared Spectroscopic Imaging:Plenary Lecture at the 5th International Conference on Advanced Vibrational Spectroscopy, 2009, Melbourne, Australia* **2010**, *64* (5), 135A−152A.

(9) Hu, L.; Chen, R.; Agarwal, K.; Sheppard, C. J. R.; Phang, J. C. H.; Chen, X. Dyadic Green's function for aplanatic solid immersion lens based sub-surface microscopy. *Opt. Express* **2011**, *19* (20), 19280−19295.

(10) Kumbham, M.; Daly, S.; O'Dwyer, K.; Mouras, R.; Liu, N.; Mani, A.; Peremans, A.; Tofail, S. M.; Silien, C. Doubling the far-field resolution in mid-infrared microscopy. *Opt. Express* **2016**, *24* (21), 24377−24389.

(11) Chan, K. L. A.; Fale, P. L. V.; Atharawi, A.; Wehbe, K.; Cinque, G. Subcellular mapping of living cells via synchrotron microFTIR and ZnS hemispheres. *Anal. Bioanal. Chem.* **2018**, *410* (25), 6477−6487.

(12) Chan, K. L. A.; Kazarian, S. G. Correcting the Effect of Refraction and Dispersion of Light in FT-IR Spectroscopic Imaging in Transmission through Thick Infrared Windows. *Anal. Chem.* **2013**, *85* (2), 1029−1036.

(13) Kner, P.; Chhun, B. B.; Griffis, E. R.; Winoto, L.; Gustafsson, M. G. L. Super-resolution video microscopy of live cells by structured illumination. *Nat. Methods* **2009**, *6* (5), 339−342.

(14) Hirvonen, L. M.; Wicker, K.; Mandula, O.; Heintzmann, R. Structured illumination microscopy of a living cell. *Eur. Biophys. J.* **2009**, *38* (6), 807−812.

(15) Yang, S.; Yan, X.; Qin, H.; Zeng, Q.; Liang, Y.; Arguello, H.; Yuan, X. *Mid-Infrared Compressive Hyperspectral Imaging* **2021**, *13* (4), 741.

(16) Phal, Y.; Pfister, L.; Carney, P. S.; Bhargava, R. Resolution Limit in Infrared Chemical Imaging. *J. Phys. Chem. C* **2022**, *126* (23), 9777−9783.

(17) Falahkheirkhah, K.; Yeh, K.; Mittal, S.; Pfister, L.; Bhargava, R. Deep learning-based protocols to enhance infrared imaging systems. *Chemometrics and Intelligent Laboratory Systems* **2021**, *217*, No. 104390.

(18) van Dijk, T.; Mayerich, D.; Bhargava, R.; Carney, P. S. Rapid spectral-domain localization. *Opt. Express* **2013**, *21* (10), 12822−12830.

(19) Frogley, M. D.; Lekkas, I.; Kelley, C. S.; Cinque, G. Performances for broadband synchrotron photothermal infrared nano-spectroscopy at Diamond Light Source. *Infrared Physics & Technology* **2020**, *105*, No. 103238.

(20) Mërtiri, A.; Jeys, T.; Liberman, V.; Hong, M. K.; Mertz, J.; Altug, H.; Erramilli, S. Mid-infrared photothermal heterodyne spectroscopy in a liquid crystal using a quantum cascade laser. *Appl. Phys. Lett.* **2012**, *101* (4), 044101.

(21) Robert, F.; Christopher, A. K.; Michael, R. P.; Viet, N.; McGill, R. A. Chemical imaging using infrared photothermal microspectroscopy. *Proc.SPIE* **2012**, *8374*, No. 837411.

(22) Atcha, T.; Shyamsunder, E.; Michelle, Y. S. Optimization of mid-IR photothermal imaging for tissue analysis. *Proc. SPIE* **2015**, *9584*, No. 95840C.

(23) Bai, Y.; Yin, J.; Cheng, J.-X. Bond-selective imaging by optically sensing the mid-infrared photothermal effect. *Sci. Adv.* **2021**, *7* (20), No. eabg1559.

(24) Pavlovetc, I. M.; Aleshire, K.; Hartland, G. V.; Kuno, M. Approaches to mid-infrared, super-resolution imaging and spectroscopy. *Phys. Chem. Chem. Phys.* **2020**, *22* (8), 4313−4325.

(25) Pavlovetc, I. M.; Podshivaylov, E. A.; Chatterjee, R.; Hartland, G. V.; Frantsuzov, P. A.; Kuno, M. Infrared photothermal heterodyne imaging: Contrast mechanism and detection limits. *J. Appl. Phys.* **2020**, *127* (16) DOI: 10.1063/1.5142277.

(26) Dazzi, A.; Glotin, F.; Carminati, R. Theory of infrared nanospectroscopy by photothermal induced resonance. *J. Appl. Phys.* **2010**, *107* (12) DOI: 10.1063/1.3429214.

(27) Dazzi, A.; Prater, C. B. AFM-IR: Technology and Applications in Nanoscale Infrared Spectroscopy and Chemical Imaging. *Chem. Rev.* **2017**, *117* (7), 5146−5173.

(28) Schwartz, J. J.; Pavlidis, G.; Centrone, A. Understanding Cantilever Transduction Efficiency and Spatial Resolution in Nanoscale Infrared Microscopy. *Anal. Chem.* **2022**, *94* (38), 13126−13135.

(29) Ramer, G.; Aksyuk, V. A.; Centrone, A. Quantitative Chemical Analysis at the Nanoscale Using the Photothermal Induced Resonance Technique. *Anal. Chem.* **2017**, *89* (24), 13524−13531.

(30) Centrone, A. Infrared Imaging and Spectroscopy Beyond the Diffraction Limit. *Annual Review of Analytical Chemistry* **2015**, *8* (1), 101−126.

(31) O'Callahan, B. T.; Yan, J.; Menges, F.; Muller, E. A.; Raschke, M. B. Photoinduced Tip−Sample Forces for Chemical Nanoimaging and Spectroscopy. *Nano Lett.* **2018**, *18* (9), 5499−5505.

(32) Lu, F.; Jin, M.; Belkin, M. A. Tip-enhanced infrared nanospectroscopy via molecular expansion force detection. *Nat. Photonics* **2014**, *8* (4), 307−312.

(33) Barlow, D. E.; Biffinger, J. C.; Cockrell-Zugell, A. L.; Lo, M.; Kjoller, K.; Cook, D.; Lee, W. K.; Pehrsson, P. E.; Crookes-Goodson, W. J.; Hung, C. S.; Nadeau, L. J.; Russell, J. N. The importance of correcting for variable probe-sample interactions in AFM-IR spectroscopy: AFM-IR of dried bacteria on a polyurethane film. *Analyst* **2016**, *141* (16), 4848−4854.

(34) Dazzi, A.; Saunier, J.; Kjoller, K.; Yagoubi, N. Resonance enhanced AFM-IR: A new powerful way to characterize blooming on polymers used in medical devices. *Int. J. Pharm.* **2015**, *484* (1), 109−114.

(35) Jahng, J.; Potma, E. O.; Lee, E. S. Tip-Enhanced Thermal Expansion Force for Nanoscale Chemical Imaging and Spectroscopy in Photoinduced Force Microscopy. *Anal. Chem.* **2018**, *90* (18), 11054−11061.

(36) Nowak, D.; Morrison, W.; Wickramasinghe, H. K.; Jahng, J.; Potma, E.; Wan, L.; Ruiz, R.; Albrecht, T. R.; Schmidt, K.; Frommer, J.; Sanders, D. P.; Park, S. Nanoscale chemical imaging by photoinduced force microscopy. *Science Advances* **2016**, *2* (3), No. e1501571.

(37) Jahng, J.; Brocious, J.; Fishman, D. A.; Huang, F.; Li, X.; Tamma, V. A.; Wickramasinghe, H. K.; Potma, E. O. Gradient and scattering forces in photoinduced force microscopy. *Phys. Rev. B* **2014**, *90* (15), No. 155417.

(38) Kenkel, S.; Gryka, M.; Chen, L.; Confer, M. P.; Rao, A.; Robinson, S.; Prasanth, K. V.; Bhargava, R. Chemical imaging of cellular ultrastructure by null-deflection infrared spectroscopic measurements. *Proc. Natl. Acad. Sci. U. S. A.* **2022**, *119* (47), No. e2210516119.

(39) Kenkel, S.; Mittal, A.; Mittal, S.; Bhargava, R. Probe−Sample Interaction-Independent Atomic Force Microscopy−Infrared Spectroscopy: Toward Robust Nanoscale Compositional Mapping. *Anal. Chem.* **2018**, *90* (15), 8845−8855.

(40) Kenkel, S.; Mittal, S.; Bhargava, R. Closed-loop atomic force microscopy-infrared spectroscopic imaging for nanoscale molecular characterization. *Nat. Commun.* **2020**, *11* (1), 3225.

(41) Jumel, J.; Taillade, F.; Lepoutre, F. J. E. P. J. A. Thermo-elastic properties characterization by photothermal microscopy*. *Eur. Phys. J. AP* **2003**, *23* (3), 217−225.

(42) Bernard, C.; Daher, N.; Bruno, C. Thermoelastic modeling: application to superresolution in photothermal and thermoelastic microscopy. *Proc. SPIE* **1997**, 466−475.

(43) Donaldson, P. M.; Kelley, C. S.; Frogley, M. D.; Filik, J.; Wehbe, K.; Cinque, G. Broadband near-field infrared spectromicroscopy using photothermal probes and synchrotron radiation. *Opt. Express* **2016**, *24* (3), 1852−1864.

(44) Morozovska, A. N.; Eliseev, E. A.; Borodinov, N.; Ovchinnikova, O. S.; Morozovsky, N. V.; Kalinin, S. V. Photothermoelastic contrast in nanoscale infrared spectroscopy. *Appl. Phys. Lett.* **2018**, *112* (3), No. 033105.

(45) Guenther, R. B.; Lee, J. W. *Partial Differential Equations of Mathematical Physics and Integral Equations*; Dover Publications: Mineola, NY, 1996.

(46) Nowacki, W. *Thermoelasticity*, 2nd ed.; Pergamon Press: Oxford, 1986.

(47) Schnell, M.; Mittal, S.; Falahkheirkhah, K.; Mittal, A.; Yeh, K.; Kenkel, S.; Kajdacsy-Balla, A.; Carney, P. S.; Bhargava, R. All-digital histopathology by infrared-optical hybrid microscopy. *Proc. Natl. Acad. Sci. U. S. A.* **2020**, *117* (7), 3388.

(48) Black, E. D.; Grudinin, I. S.; Rao, S. R.; Libbrecht, K. G. Enhanced photothermal displacement spectroscopy for thin-film characterization using a Fabry-Perot resonator. *J. Appl. Phys.* **2004**, *95* (12), 7655−7659.

(49) Samolis, P. D.; Sander, M. Y.; Hong, M. K.; Erramilli, S.; Narayan, O. Thermal transport across membranes and the Kapitza length from photothermal microscopy. *Journal of Biological Physics* **2023**, *49* (3), 365−381.

(50) Taubner, T.; Keilmann, F.; Hillenbrand, R. Nanoscale-resolved subsurface imaging by scattering-type near-field optical microscopy. *Opt. Express* **2005**, *13* (22), 8893−8899.

(51) Jung, L.; Hauer, B.; Li, P.; Bornhöfft, M.; Mayer, J.; Taubner, T. Exploring the detection limits of infrared near-field microscopy regarding small buried structures and pushing them by exploiting superlens-related effects. *Opt. Express* **2016**, *24* (5), 4431−4441.

(52) Krutokhvostov, R.; Govyadinov, A. A.; Stiegler, J. M.; Huth, F.; Chuvilin, A.; Carney, P. S.; Hillenbrand, R. Enhanced resolution in subsurface near-field optical microscopy. *Opt. Express* **2012**, *20* (1), 593−600.

(53) Goodman, J. W. *Introduction to Fourier Optics*, 2nd ed.; McGraw-Hill: New York, 1996; p xviii, p 441.

https://doi.org/10.1021/cbmi.4c00018
Chem. Biomed. Imaging 2024, 2, 413−421